Equivalent electric circuit model of accurate ion energy control with tailored waveform biasing

Citation for published version (APA):
Yu, Q., Lemmen, E., Vermulst, B., Mackus, A. J. M., Kessels, W. M. M., & Wijnands, K. (2022). Equivalent electric circuit model of accurate ion energy control with tailored waveform biasing. *Plasma Sources Science and Technology*, *31*(3), Article 035012. https://doi.org/10.1088/1361-6595/ac4c27

Document license:
CC BY

DOI:
10.1088/1361-6595/ac4c27

Document status and date:
Published: 01/03/2022

Document Version:
Publisher’s PDF, also known as Version of Record (includes final page, issue and volume numbers)

Please check the document version of this publication:

• A submitted manuscript is the version of the article upon submission and before peer-review. There can be important differences between the submitted version and the official published version of record. People interested in the research are advised to contact the author for the final version of the publication, or visit the DOI to the publisher's website.
• The final author version and the galley proof are versions of the publication after peer review.
• The final published version features the final layout of the paper including the volume, issue and page numbers.

Link to publication

General rights
Copyright and moral rights for the publications made accessible in the public portal are retained by the authors and/or other copyright owners and it is a condition of accessing publications that users recognise and abide by the legal requirements associated with these rights.

• Users may download and print one copy of any publication from the public portal for the purpose of private study or research.
• You may not further distribute the material or use it for any profit-making activity or commercial gain
• You may freely distribute the URL identifying the publication in the public portal.

If the publication is distributed under the terms of Article 25fa of the Dutch Copyright Act, indicated by the “Taverne” license above, please follow below link for the End User Agreement:

www.tue.nl/taverne

Take down policy
If you believe that this document breaches copyright please contact us at:

openaccess@tue.nl

providing details and we will investigate your claim.

Download date: 04. Oct. 2023

PAPER • OPEN ACCESS

Equivalent electric circuit model of accurate ion energy control with tailored waveform biasing

To cite this article: Qihao Yu *et al* 2022 *Plasma Sources Sci. Technol.* **31** 035012

View the article online for updates and enhancements.

You may also like

- Substructure identification for shear structures: cross-power spectral density method
Dongyu Zhang and Erik A Johnson

- Improving substructure identification accuracy of shear structures using virtual control system
Dongyu Zhang, Yang Yang, Tingqiang Wang et al.

- Loop substructure identification for shear structures of unknown structural mass using synthesized references
Dongyu Zhang and Hui Li

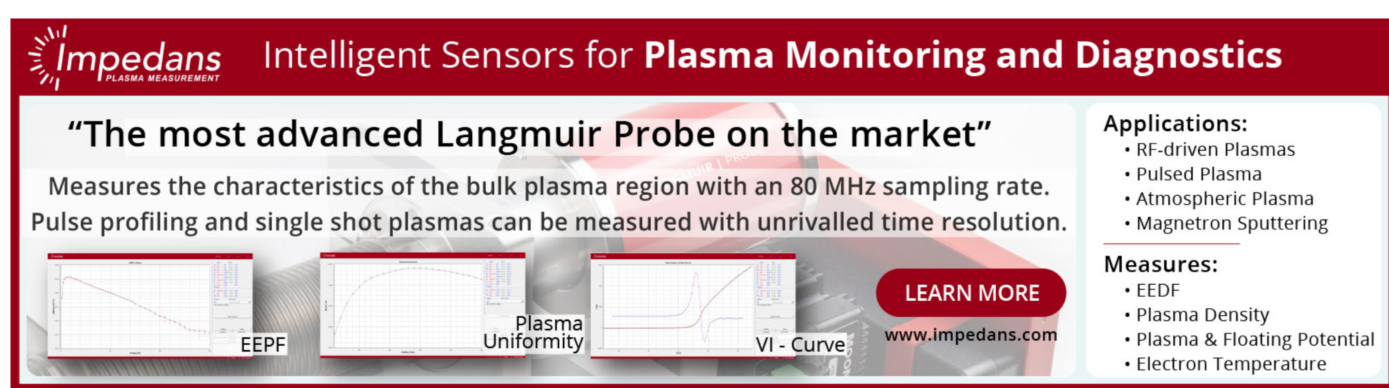

This content was downloaded from IP address 131.155.95.31 on 30/03/2022 at 09:37

Plasma Sources Science and Technology

Plasma Sources Sci. Technol. **31** (2022) 035012 (14pp) https://doi.org/10.1088/1361-6595/ac4c27

Equivalent electric circuit model of accurate ion energy control with tailored waveform biasing

Qihao Yu (余骑浩)[1,*], Erik Lemmen[1], Bas Vermulst[1,*], Adriaan J M Mackus[2], Wilhelmus M M (Erwin) Kessels[2] and Korneel Wijnands[1]

[1] Department of Electrical Engineering, Eindhoven University of Technology, PO Box 513, The Netherlands

[2] Department of Applied Physics, Eindhoven University of Technology, PO Box 513, The Netherlands

E-mail: q.yu@tue.nl and b.j.d.vermulst@tue.nl

Received 24 September 2021, revised 20 December 2021
Accepted for publication 17 January 2022
Published 9 March 2022

Abstract

For atomic scale plasma processing involving precise, (an)isotropic and selective etching and deposition, it is required to precisely control the energy of the plasma ions. Tailored waveforms have been employed to bias the substrate table to accurately control this ion energy. Recent research has shown that switched-mode power converters can be used to generate this kind of waveform, with the benefit of increased energy efficiency and flexibility compared to the traditionally used linear amplifiers. In this article, an improved equivalent electric circuit model of the plasma reactor is proposed to allow simulation and bias waveform optimization. The equivalent electric circuit is analysed for different process phases, including the charge, discharge, and post-discharge phase. The proposed model is suitable for electric circuit simulation and can be used for predicting the electric waveforms and ion energy distributions. Plasma parameters are required as input for the model, thus an empirical parameter identification method based on the electrical measurements of the bias voltage and output current waveforms is introduced. Since these electrical measurements do not interact with the plasma process, the proposed parameter identification method is nonintrusive. Experiments have been carried out, which demonstrate that the proposed model and parameter identification method provide the expected accuracy.

Keywords: atomic layer etching, atomic layer deposition, equivalent electric circuit, ion energy distribution, switched-mode power converter, tailored waveform biasing

(Some figures may appear in colour only in the online journal)

1. Introduction

Plasma processing is crucial in semiconductor manufacturing, such as plasma etching and deposition to fabricate nanodevices. With the size of integrated circuits (ICs) continuing to shrink, atomic scale processing, including atomic layer etching (ALE) and atomic layer deposition (ALD), turns to be vital since these methods can offer high selectivity, precise thickness control and 3D processing of the materials [1]. Taking plasma ALE for example, the thickness of the etched material is precisely controlled by the use of the self-limiting reactions. During such an ALE process, the substrate surface is typically first exposed to the reactive species to weaken the binding energy between the surface and bulk atoms of the substrate [2]. The goal of this step is to modify the surface so that the surface atoms can be removed without affecting the underlying material [3]. After that, energetic plasma ions bombard

* Authors to whom any correspondence should be addressed.

Original content from this work may be used under the terms of the Creative Commons Attribution 4.0 licence. Any further distribution of this work must maintain attribution to the author(s) and the title of the work, journal citation and DOI.

 © 2022 The Author(s). Published by IOP Publishing Ltd

the modified substrate surface [4]. The ions should carry sufficient energy such that they can break the weakened bonds and knock out the surface atoms. Meanwhile, the energy of the ions should not exceed the threshold for etching the underlying bulk material. Therefore, the ion energy distribution (IED) should fall into a narrow window to achieve such etch selectivity. Under some circumstances, this energy window can be as narrow as 10 eV such as the plasma ALE of Ge by using Cl_2 plasma for surface modification [5].

Figure 1 shows a schematic representation of a typical inductively coupled plasma (ICP) reactor often employed for ALE. It shows the common case that the substrate is smaller than the table, for which part of the table is also exposed to the plasma. As shown in figure 1, gas is infused from the top, and the plasma is ignited and sustained in the chamber by an external radio-frequency (RF) power source through a matching network unit. The pressure in the chamber is kept low. This reduces the particle collisions in the plasma sheath near the substrate surface, allowing for ion bombardment. To do so, often, a power converter is connected to the table, which generates a negative voltage on the substrate surface. As a result, the ions in the bulk plasma are accelerated towards the table, and bombard the substrate surface to remove the target material. Moreover, the normal direction of ion bombardment to the substrate surface enables anisotropic etching.

Ion energy can be controlled by biasing the substrate surface voltage with a power converter. A narrow IED calls for a quasi-constant substrate surface voltage potential. For a conductive substrate, the ion energy can be controlled by a dc bias voltage. However, for a dielectric substrate, there is an equivalent substrate capacitance [6]. The bombarding ions are accumulated on the substrate surface, thus the voltage potential of the substrate surface increases, known as the charging effect, leading to a broad IED.

Different techniques have been studied targeting a narrow IED for the dielectric substrates. In traditional single-frequency capacitively coupled plasmas (CCPs), a single power source is used to control the ion density, ion flux, ion energy and other plasma properties, which can easily lead to plasma nonuniformity [7, 8] and makes it hard to accurately control the ion energy independently of ion flux [9]. Dual-frequency CCPs were therefore proposed [10, 11]. It uses a high-frequency RF source to mainly control ion flux and an RF source of lower frequency to control ion energy separately. It offers a better plasma uniformity over large surface areas compared to the single-frequency CCPs [12]. However, the coupling effect of the two RF sources can cause issues such as substrate damage or reduced etching rate [13]. A better decoupled control of ion flux and ion energy in dual-frequency CCPs can be obtained by controlling the phase shift between two fixed-frequency RF sources utilizing the electrical asymmetry effect, as done in [14–17]. Moreover, other voltage waveform tailoring techniques, such as using a low-frequency square waveform with high-frequency harmonics [18, 19], have also been developed for CCPs.

Compared to CCPs, ICPs enjoy the benefit of higher plasma density. ICPs are the focus of this article. In such ICP, the RF

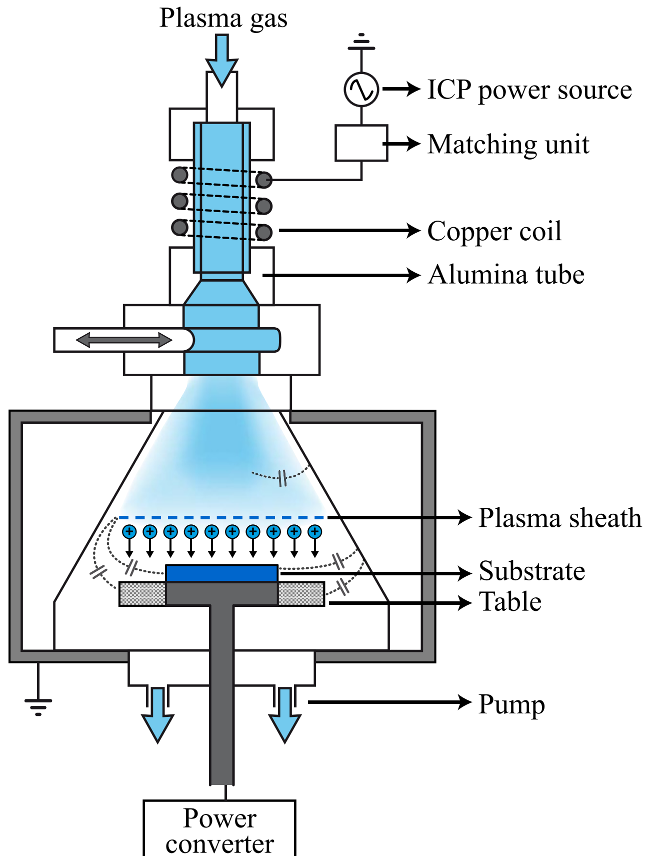

Figure 1. A typical setup of an ICP reactor. The solid part of the table is covered by the substrate while the gridded part is directly exposed to the plasma. The height of the plasma sheath near the substrate surface is much smaller than the dimension of the reactor. It is exaggerated here for better visualization.

power is inductively coupled to the plasma across a dielectric window, which yields a low plasma floating potential of typically 20 to 40 V with respect to the substrate and enables better decoupled control of ion flux and ion energy [9]. Different biasing techniques for ICPs have been studied [20–22], including RF biasing [23–25], pulse-shaped biasing [26–28], and tailored waveform biasing [29–33], the voltage waveforms of which are shown in figures 2(a)–(c), respectively. The negative parts of all the three biasing waveforms are used to create a negative voltage potential on the substrate surface to enhance ion energy. The bombarding ions are charging the substrate capacitance during this time. Therefore, to prevent overvoltage on the substrate, a short positive voltage is applied to attract the electrons and reset the voltage potential periodically, i.e. discharging the substrate.

The RF biasing creates a sinusoidal voltage potential on the substrate surface, thus generating a broad and bimodal IED as depicted in figure 3 [34, 35], which is not preferred in atomic scale processing. Although increasing the RF biasing frequency helps narrowing the IED, it is limited by the ion mass and it is much less effective for light ions such as hydrogen. Furthermore, a sufficiently large biasing frequency makes the RF wavelength comparable to the substrate dimension, and this can cause severe nonuniformities [23]. The

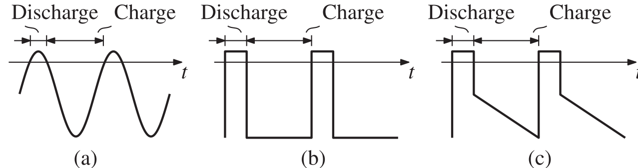

Figure 2. (a) RF biasing voltage waveform. (b) Pulse-shaped biasing voltage waveform. (c) Tailored waveform biasing voltage waveform.

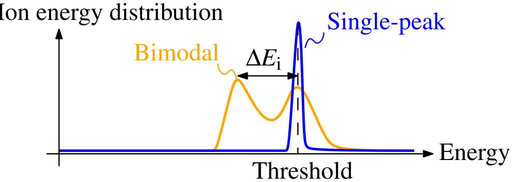

Figure 3. Bimodal and single-peak IED.

pulse-shaped biasing could deliver a narrow single-peak IED as depicted figure 3 under specific conditions, specially for a dielectric substrate with large capacitance. However, the IED is heavily distorted if the substrate capacitance is small, since a small substrate capacitance leads to a large voltage potential rise due to the charging effect, thus resulting in a broad IED [30]. Although increasing pulse-shaped biasing frequency can reduce this charging effect as well, similar drawbacks occur as for increasing the RF biasing frequency. Compared to the pulse-shaped biasing, tailored waveform biasing uses a negative voltage slope to compensate the charging effect. The voltage slope rate should be well tuned, the value of which is determined by the properties of the substrate and the ion flux. Under this circumstance, the voltage potential of the substrate bottom is linearly decreasing, thus the substrate surface potential remains quasi-constant. Tailored waveform biasing requires a significantly reduced repetition frequency compared to the RF biasing and pulse-shaped biasing. The capability of accurate ion energy control makes tailored waveform biasing well-suited for the highly-selective atomic scale processing.

Traditionally, the tailored waveform is generated by class-A linear amplifiers, which are typically energy inefficient. In addition, a tuned matching network is necessary in order to match the impedance of the linear amplifier and the plasma reactor [25]. Recently, switched-mode power converters (SMPCs) have been applied to generate the tailored waveform, which have a significantly higher energy efficiency compared to the linear amplifier [36]. It also advantageously omits the matching network since the converter operates in a quasi-dc mode. The bias waveform can be actively and flexibly tailored by this converter, with controllable pulse magnitude and voltage slope rate. The SMPC brings huge convenience and flexibility to the tailored waveform biasing. However, for electrical engineers, an equivalent electric circuit (EEC) model of the reactor is needed to conduct circuit simulations and optimize the electrical design. For plasma physicists, it is also desired to combine the simulation of the bias converter and the plasma reactor to predict the IED and optimize the bias waveform. A complete EEC model of the reactor enables this combined simulation on the circuit level, which tremendously reduces the computation time compared to a traditional plasma simulation method like particle-in-cell (PIC).

Although some reactor models have been derived in previous research, most of them are used for RF biasing [9, 25, 32, 37–39] or are a steady-state simplification of tailored waveform biasing [36, 40, 41]. These models cannot be directly used for transient analysis in tailored waveform biasing because the discharge process is not accurately included. In [42], a modified model is proposed, which emulates the discharge process by a virtual sheath reset circuit. While this modified model can roughly represent the charge and discharge processes, and thus can be used for electric circuit simulation, it significantly increases the complexity of the circuit. In this article, an improved EEC model is introduced with detailed analysis of the transient response during the charge, discharge, and post-discharge phase.

Parameters of the EEC model, including the values of the capacitors and currents, are required in order to fulfil circuit simulation and IED prediction. Typically these parameters are derived from plasma physics theory. However, the derived parameters can be variant and nonlinear, which unnecessarily increases the complexity of the model [25]. Furthermore, the determination of some parameters demands intrusive measurements of plasma properties, such as measuring the ion density with a Langmuir probe [43]. In this research, a parameter identification method is introduced, which linearizes the electric parameters in the model within the operating range. The method is fully based on nonintrusive electrical measurements, being the voltage and current waveforms on the power converter side.

With the proposed model and the parameter identification method, a plasma reactor can be simulated in a typical circuit simulation software, such as SPICE or MATLAB/Simulink. Both the electric waveforms and the IEDs are predicted with the simulation model by applying the same bias voltage waveforms as applied to the plasma reactor. In this article, the predicted waveforms and IEDs are compared to the experimental measurements obtained from a plasma reactor for verification.

The structure of this paper is as follows: first, the EEC models, including the traditional model and the improved model are derived in section 2, followed by the parameter identification method in section 3. Next, the experimental validation is carried out and discussed in section 4. Finally, section 5 concludes the paper.

2. Reactor model

2.1. Traditional EEC model of the plasma reactor

In a typical ICP reactor, the bulk plasma is confronted with two major surfaces, which are the grounded reactor wall and the substrate table that can be biased. The area of the reactor wall is larger than that of the table. Therefore, the plasma reactor can be simplified as an asymmetrical parallel plate system as depicted in figure 4(a). In most cases, a dielectric substrate is

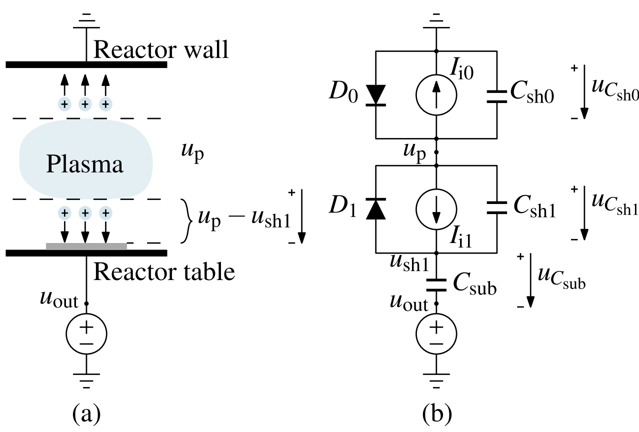

Figure 4. (a) Parallel plate system representation of the plasma reactor. (b) Traditional EEC model of the plasma reactor.

used, as presented by the grey area in the figure. The traditional EEC model focuses on RF biasing as described in [9, 25, 32, 37–39], which can be generalized by the EEC model shown in figure 4(b). In this model, two sheaths are formed between the plasma and reactor wall, and the plasma and substrate, respectively. Each sheath is modelled by a constant current source, a sheath capacitor and a diode in parallel. The current sources account for the equivalent currents generated by bombarding ions. The dielectric substrate is modelled by a capacitor C_{sub}. u_p is the plasma potential and u_{sh1} is the substrate surface potential.

In the RF biasing case, a blocking capacitor is used between the power converter and the table, and a self-biased voltage is formed over the blocking capacitor, which is omitted in figure 4 for simplicity. The self-biased voltage is caused by the initial unbalance between the inflow and outflow current. After reaching the steady-state, the net current flowing through the blocking capacitor is zero in each repetition period and the voltage over the blocking capacitor can be considered constant [44]. It should be noted that u_{out} here can be seen as the bias voltage after the blocking capacitor. Therefore, it can be described by

$$u_{out} = V_{rf}\,\sin(2\pi f_{rf} t) - V_b, \tag{1}$$

where V_{rf} is the magnitude of the RF voltage, f_{rf} is the RF frequency and V_b is the dc voltage over the blocking capacitor. The bombarding ions enter the sheath with an initial energy equal to $eu_p = -eu_{C_{sh0}}$, where e is the elementary charge. For simplicity, it is assumed for now that the sheath thickness is negligible so that the ion transit time in the sheath is much smaller than the RF period. As a result, the extra energy ions obtained in the sheath by the acceleration in electric field is equal to $eu_{C_{sh1}}$, determined by the instantaneous value of $u_{C_{sh1}}$ at the moment when ions enter the sheath.

During the steady-state RF biasing, C_{sh0}, C_{sh1} and C_{sub} constitute a capacitive voltage divider. As a result, the voltage over those capacitors is determined by

$$\begin{pmatrix} u_{C_{sh0}} \\ u_{C_{sh1}} \\ u_{C_{sub}} \end{pmatrix} = \begin{pmatrix} V_0 \\ V_1 \\ V_{sub} \end{pmatrix} - \begin{pmatrix} \frac{1}{C_{sh0}} \\ \frac{1}{C_{sh1}} \\ \frac{1}{C_{sub}} \end{pmatrix} \cdot \frac{V_{rf}\,\sin(2\pi f_{rf} t)}{\frac{1}{C_{sh0}}+\frac{1}{C_{sh1}}+\frac{1}{C_{sub}}}, \tag{2}$$

where V_0, V_1 and V_{sub} are the dc offset voltages over C_{sh0}, C_{sh1} and C_{sub}, respectively. The value of V_0, V_1 and V_{sub} are determined by the bias voltage waveform and the capacitance values. According to Kirchhoff's voltage law, they are governed by

$$V_0 + V_1 + V_{sub} = V_b. \tag{3}$$

Since $u_{C_{sh0}}$ cannot be positive and $u_{C_{sh1}}$ cannot be negative due to the diodes, V_0 and V_1 should guarantee

$$\begin{cases} V_0 \leqslant -\dfrac{\frac{1}{C_{sh0}}}{\frac{1}{C_{sh0}}+\frac{1}{C_{sh1}}+\frac{1}{C_{sub}}} V_{rf} \\ V_1 \geqslant \dfrac{\frac{1}{C_{sh1}}}{\frac{1}{C_{sh0}}+\frac{1}{C_{sh1}}+\frac{1}{C_{sub}}} V_{rf} \end{cases}. \tag{4}$$

The ions bombarding the substrate surface with an ion energy $E_i(t) = e\left(u_p(t) + u_{C_{sh1}}(t)\right)$, which can be described by

$$E_i(t) = \frac{\frac{1}{C_{sh0}} - \frac{1}{C_{sh1}}}{\frac{1}{C_{sh0}}+\frac{1}{C_{sh1}}+\frac{1}{C_{sub}}} V_{rf}\,\sin(2\pi f_{rf} t) + V_1 - V_0. \tag{5}$$

Since the asymmetrical sheath yields $C_{sh0} \neq C_{sh1}$ [39], the bombarding ions have an average energy equal to $e(V_1 - V_0)$ and an energy variance ΔE_i equal to

$$\Delta E_i = eV_{rf}\left|\frac{\frac{1}{C_{sh0}} - \frac{1}{C_{sh1}}}{\frac{1}{C_{sh0}}+\frac{1}{C_{sh1}}+\frac{1}{C_{sub}}}\right|. \tag{6}$$

This results in a bimodal IED as shown in figure 3. In practice, ion transition in the sheath takes time. Therefore, the extra energy ions obtain in the sheath is the average of $eu_{C_{sh1}}(t)$ over the ion transit time. This effect can reduce the width of IED.

The traditional EEC model is able to explain the RF biasing while it cannot be directly used for the tailored waveform biasing. In the tailored waveform biasing, bombarding ions are accumulated on the substrate surface and charging C_{sub} when a negative voltage slope is applied to the table, as depicted in figure 2(c). C_{sub} should be periodically discharged by a positive voltage pulse to avoid over voltage. During the positive voltage pulse, fast-moving electrons are attracted, thereby discharging the capacitors rapidly. However, in the traditional EEC model, the capacitors can only be discharged through the current sources I_{i0} and I_{i1}. The ion current is significantly smaller than the electron current, resulting in a slow discharge process in this model. Furthermore, the discharge electron current decays exponentially as depicted in [30], which cannot be realized by the constant current sources.

Besides, after the positive discharge voltage, denoted by V_d in this article, is applied and the circuit reaches its steady-state,

the voltage of C_{sub} should be fully discharged to zero. The voltage potential of the substrate surface should be V_d. Consequently, the substrate surface has a higher voltage potential compared to the grounded reactor wall. The plasma potential u_p is determined by the surface with a higher voltage potential [45] as

$$u_p = V_d + V_p. \tag{7}$$

Here V_p is the floating potential of the plasma. The voltage of C_{sh1} should represent the voltage over this sheath, thus it is close to zero since the floating potential V_p is typically small [9]. However, due to the capacitive voltage divider formed by C_{sh0}, C_{sh1} and C_{sub} as shown in figure 4(b), the capacitors cannot be completely discharged when $u_{out} = V_d$ according to Kirchhoff's voltage law. Instead, voltage drops over C_{sub} and C_{sh1} remain positive, the magnitudes of which are determined by V_d. As a result, the steady-state obtained in the traditional model deviates from the practice. Therefore, a different EEC is required to model tailored waveform biasing.

2.2. Proposed improved EEC model of the plasma reactor

An improved EEC model is proposed as depicted in figure 5. An extra sheath is formed between the exposed part of the table (as depicted by the gridded part in figure 1) with the plasma. This extra sheath is seldom discussed in previous research but it is essential, especially for the existence of the diode D_2. The diode D_2 provides an extra path during discharge so that C_{sh1} and C_{sub} can be fully discharged when the positive discharge voltage V_d is applied and D_2 is conducting. Since the reactor is always grounded and the sheath between plasma and the reactor wall is not of interest, this sheath is omitted for simplicity. Meanwhile, a resistor R_p is used to represent the bulk plasma and provide a fast RC discharge path, which is exponentially decaying. Besides, there exist parasitic capacitors between the table and the reactor wall, the substrate and the reactor wall, as also shown in figure 1. Those capacitors are modelled as a lumped table capacitor C_t. L_s is the stray inductance in the power converter and the table connection.

The modelled process can be divided into three individual phases as shown in figure 6, i.e. the charge phase, the discharge phase, and the post-discharge phase. The part of the tailored waveform when the table is negatively biased is defined as the charge phase since the ions are accumulating on the substrate surface and charging the substrate capacitor during this time. When a positive voltage V_d is applied to the table, the capacitors are discharged within a short time, which is defined by the discharge phase. After the capacitors are fully discharged, the positive voltage can be held for a short time, which is defined by the post-discharge phase. Each phase is analysed in detail in this section. The waveform of u_t is the so-called tailored waveform. The target of the SMPC is to generate a voltage waveform u_{out} in order to obtain the desired u_t.

2.2.1. Charge phase.

The ion energy is required to remain in a specific narrow window for processing with high selectivity. Therefore, u_{sh1} is desired to be a negative constant value. Since ions are accumulated and charging the substrate, this phase is designated as charge phase. From the EEC model, u_{sh1} is determined by

$$C_{sub}\frac{d(u_{sh1}-u_t)}{dt} = I_{i1} + C_{sh1}\frac{d\left(u_p-u_{sh1}\right)}{dt}. \tag{8}$$

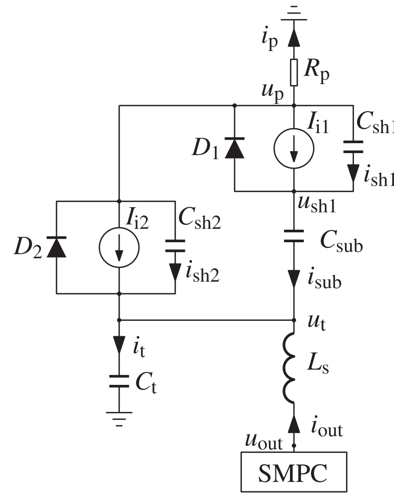

Figure 5. The improved EEC model of the plasma reactor.

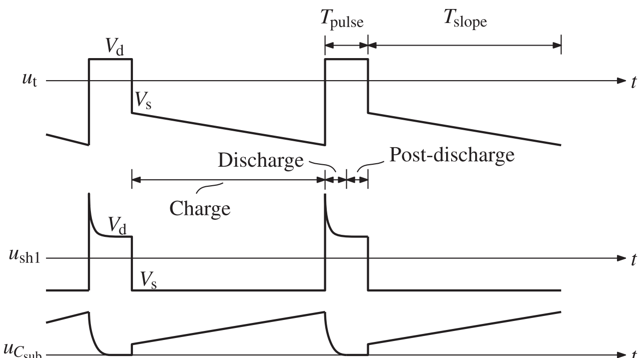

Figure 6. The typical waveforms of u_t, u_{sh1}, and $u_{C_{sub}}$, which can be divided into the charge, discharge, and post-discharge phases.

During charging when the reactor table is negatively biased, the grounded reactor wall has a higher voltage potential than the table. The plasma potential is determined by the surface with the higher voltage potential [45]. Therefore, in practice, the plasma has a positive potential V_p with respect to ground. Since this voltage is relatively small compared to the bias voltage, it is omitted here for simplicity. In the model, the plasma potential u_p is determined by

$$u_p = R_p i_p = -R_p\left(I_{i1} + I_{i2} + i_{sh1} + i_{sh2}\right), \tag{9}$$

which yields a negative value during the charge phase. Therefore, R_p should be sufficiently small during this phase, so that $u_p \approx 0$. I_{i1} is causing charge accumulation on C_{sub} and should be compensated. As a result, a constant u_{sh1} requires a voltage slope on u_t defined by

$$\frac{du_t}{dt} = -\frac{I_{i1}}{C_{sub}}. \tag{10}$$

In other words, u_t should linearly decrease with a slope rate of $-I_{i1}C_{sub}^{-1}$ to exactly compensate the ion charge accumulation effect for a constant ion energy [26]. Assuming the duration of the voltage slope is T_{slope} (as annotated in figure 6), the magnitude of the voltage change ΔV during the charge phase is given by

$$\Delta V = \frac{du_t}{dt}T_{slope} = -\frac{I_{i1}}{C_{sub}}T_{slope}. \quad (11)$$

Contrastingly, for pulsed-shape biasing as depicted in figure 2, the charge effect is not compensated and the substrate surface could rise by $|\Delta V|$ during the charge phase. A small C_{sub} or a large charging time (low repetition frequency) could lead to large voltage rise and a broad IED.

In this article, the condition that (10) is achieved is defined as the optimal operating point. Consequently, the EEC model in figure 5 can be simplified as shown in figure 7(a) during the charge phase.

2.2.2. Discharge phase. Because C_{sub} is continuously charging during the charge phase, it is required to discharge it periodically to avoid over-voltage on the substrate. By applying a positive voltage pulse to the table, both the substrate and table sheath are restructured and reformed. The capacitor C_{sh1}, C_{sh2} and C_{sub} are discharged by attracting the electrons instantly, which is realized by RC discharge through resistor R_p in the circuit model.

First, $u_{C_{sh1}}$ is positive, thus diode D_1 is blocking. C_{sub} is discharging through C_{sh1}. The equivalent circuit representing the moment when C_{sh1} is not fully discharged is shown in figure 7(b).

After C_{sh1} is fully discharged, $u_{C_{sh1}}$ turns to zero and D_1 is conducting. C_{sub} is discharging through D_1. The ion current I_{i1} is completely flowing through D_1. The equivalent circuit representing the moment after C_{sh1} is fully discharged is shown in figure 7(c). Since C_{sub} and C_{sh2} are in parallel, both capacitors should be fully discharged at the same time.

The RC discharge process represents the sheath collapsing. The discharge current in the loop is decaying exponentially. Normally this process happens in a short time up to hundreds of nanoseconds [30].

2.2.3. Post-discharge phase. After C_{sh2} and C_{sub} are fully discharged, the voltages over C_{sh1}, C_{sh2} and C_{sub} become zero and D_2 is conducting. The plasma potential u_p is then clamped to the discharge voltage V_d in this case. The ion current I_{i2} is completely flowing through D_2. The equivalent circuit at this moment is shown in figure 7(d).

The post-discharge phase is preferred to be short such that the ion energy is well defined during the most of the duration of the waveform, thereby increasing the throughput. On the other hand, the post-discharge phase is a degree of freedom to adjust the bias waveform repetition period. The time duration of the charge phase T_{slope} is rather fixed because ΔV is limited by the output capacity of the power converter. The time duration of the discharge phase is determined by the plasma properties and the operating condition, thus it cannot be controlled. By controlling the duration of the post-discharge phase, the bias waveform repetition period (and the frequency) can be flexibly tailored. The total time duration of the discharge phase and the post-discharge phase is denoted by T_{pulse} as shown in figure 6.

After the post-discharge phase is finished, a negative voltage pulse should be applied to the table to restart the charge phase. The magnitude of this voltage pulse determines the ion energy. Assuming u_t changes from discharge V_d to a negative start voltage V_s, it must be stressed that before u_t turns negative, D_2 is conducting and the voltages over C_{sh1}, C_{sh2} and C_{sub} are clamped to zero. Only after u_t is below zero, D_2 is blocking and the equivalent circuit turns from figures 7(d) to (a) again by rapidly recharging C_{sh1}, C_{sh2} and C_{sub} through R_p. It should be noted that this recharging process also takes time comparable to the discharge phase. However, since its equivalent circuit is the same as the charge phase, it is not separately classified for brevity. Due to the capacitive voltage divider formed by C_{sh1} and C_{sub}, u_{sh1} obtains an initial value at the beginning of the charge phase governed by

$$u_{sh1} = \frac{C_{sub}}{C_{sub} + C_{sh1}}V_s. \quad (12)$$

Since C_{sub} is typically much larger than C_{sh1}, u_{sh1} can be approximate by V_s.

3. Parameter identification

In order to conduct circuit simulation, the parameters of the EEC model should be accurately identified. In this section, a parameter identification method is introduced, which is fully based on the nonintrusive electrical measurements. Specifically, only the waveforms of u_{out} and i_{out} are required. In practice, the sheath capacitance C_{sh1} and C_{sh2}, the ion current I_{i1} and I_{i2} are nonlinear and voltage dependent. If and only if the optimal operating point is achieved, u_{sh1} and C_{sh1} can remain constant during the charge phase [25]. In this work, these parameters are assumed to be constant around the optimal operating point for simplicity. In addition, C_{sub} is assumed to be constant since the processing depth of the substrate is neglectable compared to its height. C_t can also be assumed to be constant since the area and distance of each surface remain basically unchanged.

During the charge phase as depicted in figure 7(a), the reactor system with the converter can be generalized by

$$i_{out} = \left(\frac{C_{sh1}C_{sub}}{C_{sh1} + C_{sub}} + C_{sh2} + C_t\right)\frac{du_t}{dt} - \frac{C_{sub}}{C_{sub} + C_{sh1}}I_{i1} - I_{i2}. \quad (13)$$

By varying the voltage slope $\frac{du_t}{dt}$, the output current i_{out} changes accordingly. With a fixed $\frac{du_t}{dt}$, i_{out} can be treated as constant during the charge phase. u_t can then be approximated by u_{out} despite the presence of L_s. Normally, the value of C_{sh2} and I_{i2} are relatively small so they are assumed to be zero in this section. Therefore, a simplified description of the system is given by

$$i_{out} = \left(\frac{C_{sh1}C_{sub}}{C_{sh1} + C_{sub}} + C_t\right)\dot{u}_{out} - \frac{C_{sub}}{C_{sub} + C_{sh1}}I_{i1}, \quad (14)$$

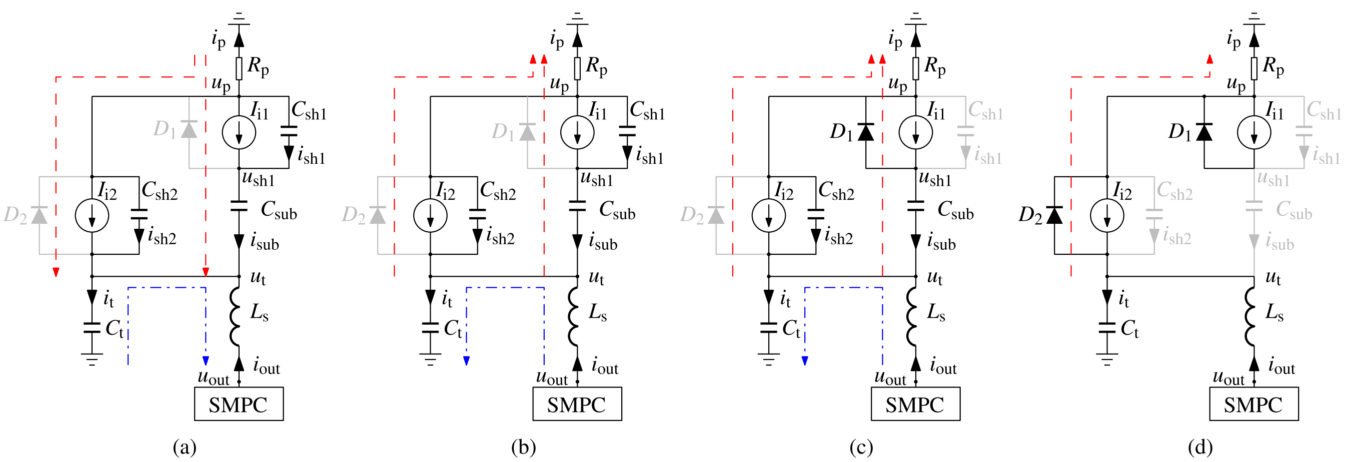

Figure 7. The equivalent circuit of the plasma reactor during (a) the charge phase, (b) the discharge phase when $u_{C_{\mathrm{sh1}}}$ has not been fully discharged, (c) the discharge phase when $u_{C_{\mathrm{sh1}}}$ has been fully discharged, and (d) the post-discharge phase when all the capacitors have been fully discharged. The dashed arrows indicate the net current direction through the corresponding sheath. The dash doted arrows indicate the current direction through C_{t}.

where $\dot{u}_{\mathrm{out}} = \frac{du_{\mathrm{out}}}{dt}$. The effective capacitance C_{eff} and effective current I_{eff} can be defined by

$$C_{\mathrm{eff}} = \frac{C_{\mathrm{sub}}}{C_{\mathrm{sh1}} + C_{\mathrm{sub}}} C_{\mathrm{sh1}} + C_{\mathrm{t}} \tag{15}$$

and

$$I_{\mathrm{eff}} = -\frac{C_{\mathrm{sub}}}{C_{\mathrm{sub}} + C_{\mathrm{sh1}}} I_{\mathrm{i1}} = \left(\frac{C_{\mathrm{sh1}}}{C_{\mathrm{sh1}} + C_{\mathrm{sub}}} - 1 \right) I_{\mathrm{i1}}. \tag{16}$$

Note that both C_{eff} and I_{eff} are variant at different operating points and they are dependent of $\dot{u}_{\mathrm{out}}$. In the identification procedure, a set of different output voltage slopes $\dot{u}_{\mathrm{out},x}$ $(x = 1, 2, 3, \ldots, n)$ with a sufficiently small step size should be applied, and the resultant output current $i_{\mathrm{out},x}$ $(x = 1, 2, 3, \ldots, n)$ during the charge phase should be measured. As a result, the value of C_{eff} and I_{eff} at the corresponding $\dot{u}_{\mathrm{out}}$ can be approximated by

$$C_{\mathrm{eff},x} = \frac{i_{\mathrm{out},x+1} - i_{\mathrm{out},x}}{\dot{u}_{\mathrm{out},x+1} - \dot{u}_{\mathrm{out},x}} \tag{17}$$

and

$$I_{\mathrm{eff},x} = \frac{\dot{u}_{\mathrm{out},x} i_{\mathrm{out},x+1} - \dot{u}_{\mathrm{out},x+1} i_{\mathrm{out},x}}{\dot{u}_{\mathrm{out},x+1} - \dot{u}_{\mathrm{out},x}}. \tag{18}$$

If $\dot{u}_{\mathrm{out},x}$ $(x = 1, 2, 3, \ldots, n)$ covers a sufficiently large range, the optimal operating point can be found. Assuming the optimal operating point is found at $x = k$, $\dot{u}_{\mathrm{out},k}$ should be equal to $-I_{\mathrm{i1}} C_{\mathrm{sub}}^{-1}$ according to (10). Under this circumstance, u_{sh1} is constant and there is no current flowing through the modelled sheath capacitor C_{sh1}. C_{sh1} can be omitted in the circuit depicted in figure 7(a). Consequently, the system can be equivalently simplified as

$$i_{\mathrm{out}} = C_{\mathrm{t}} \dot{u}_{\mathrm{out}} - I_{\mathrm{i1}}. \tag{19}$$

This simplification can also be derived by substituting $\dot{u}_{\mathrm{out}} = -I_{\mathrm{i1}} C_{\mathrm{sub}}^{-1}$ in to (14), because essentially (19) is a special point of the generalized system depicted by (14). Since

$$C_{\mathrm{t}} \leqslant C_{\mathrm{eff}} = \frac{C_{\mathrm{sub}}}{C_{\mathrm{sh1}} + C_{\mathrm{sub}}} C_{\mathrm{sh1}} + C_{\mathrm{t}} \tag{20}$$

and

$$-I_{\mathrm{i1}} \leqslant I_{\mathrm{eff}} = -\frac{C_{\mathrm{sub}}}{C_{\mathrm{sub}} + C_{\mathrm{sh1}}} I_{\mathrm{i1}} \tag{21}$$

always stand, the value of C_{t} and I_{i1} can be obtained by finding the minimum effective capacitance and current as

$$C_{\mathrm{t}} = \min\left(C_{\mathrm{eff},x}\right) = C_{\mathrm{eff},k} \tag{22}$$

and

$$I_{\mathrm{i1}} = -\min\left(I_{\mathrm{eff},x}\right) = -I_{\mathrm{eff},k}, \tag{23}$$

respectively. It should be pointed out that I_{i1} can also be calculated from (19) after finding C_{t}. While theoretically the minimum of the effective capacitance and current should be achieved at the same $\dot{u}_{\mathrm{out}}$, both methods should give the same result.

The above analysis utilizes the special format of the proposed circuit model at the optimal operating point to calculate the exact value of C_{t} and I_{i1}. The benefit of this method is that the value of C_{sh1} and C_{sub} are not required, meaning the method is immune of the nonlinear C_{sh1} effect. Therefore, the identification of C_{t} and I_{i1} are expected to be accurate. Nonetheless, the value of C_{sh1} has to be linearised and assumed to be constant within the covered range of $\dot{u}_{\mathrm{out},x}$ $(x = 1, 2, 3, \ldots, n)$. Defining a constant equivalent capacitance and current by

$$C_{\mathrm{eq}} = \frac{C_{\mathrm{sh1}} C_{\mathrm{sub}}}{C_{\mathrm{sh1}} + C_{\mathrm{sub}}} + C_{\mathrm{t}} \tag{24}$$

and

$$I_{\mathrm{eq}} = \frac{C_{\mathrm{sub}}}{C_{\mathrm{sub}} + C_{\mathrm{sh1}}} I_{\mathrm{i1}}, \tag{25}$$

(14) can be rewritten as

$$i_{\mathrm{out}} = C_{\mathrm{eq}} \dot{u}_{\mathrm{out}} - I_{\mathrm{eq}}. \tag{26}$$

A linear regression can be determined within the operating range, which is able to find the value of C_{eq} and I_{eq} by least squares method by minimizing the function

$$f(C_{eq}, I_{eq}) = \sum_{x=1}^{n} \left(C_{eq}\dot{u}_{out,x} - I_{eq} - i_{out,x}\right)^2. \quad (27)$$

Based on the practical measurements, typically C_{sub} (typically of nanofarad magnitude) is much larger than the sheath capacitance (typically of sub-nanofarad magnitude), (24) can be further approximated by

$$C_{eq} \approx C_{sh1} + C_t. \quad (28)$$

As a result, linearised C_{sh1} can be calculated by

$$C_{sh1} = C_{eq} - C_t. \quad (29)$$

C_{sub} can be further solved from (25), yielding to

$$C_{sub} = \frac{C_{sh1} I_{eq}}{I_{i1} - I_{eq}}. \quad (30)$$

Up to now, the parameters essential for the charge phase have been completely extracted. On the other hand, during the discharge phase, there is a resonance in transient response with a frequency of f_r in the loop. This resonance comes from the LC network formed by the plasma reactor and the stray inductance L_s. The value of L_s can be determined by

$$L_s = \frac{1}{4\pi^2 f_r^2 (C_t + C_{sub})} \quad (31)$$

when the optimal operating point is achieved.

During the discharge phase, capacitor C_{sh1}, C_{sh2} and C_{sub} should be discharged within hundreds of nanoseconds through resistor R_p. Therefore, during this phase R_p can be approximated by

$$R_p = \frac{\tau}{C_{sub}}, \quad (32)$$

where τ is the time constant of the RC circuit. Based on the RC discharge circuit, it takes about 2.3τ to discharge the capacitor voltage to 10% of the initial value. Since the sheath collapsing and reforming takes up to hundreds of nanoseconds, a typical value of τ can be tens of nanoseconds.

During the post-discharge phase, the output current is determined by

$$i_{out} = \frac{V_d}{R_p}. \quad (33)$$

Since the net output current of the converter should be balanced due to the blocking capacitor, and the net current through all the capacitors are zero due to the periodic capacitor voltages, the output current during the post-discharge phase should be governed by

$$i_{out} = \frac{T_{slope}}{T_{pulse}} I_{i2}. \quad (34)$$

As a result, the plasma resistor R_p can be obtained by

$$R_p = \frac{T_{pulse} T_{slope}}{T_{pro} I_{i2}}. \quad (35)$$

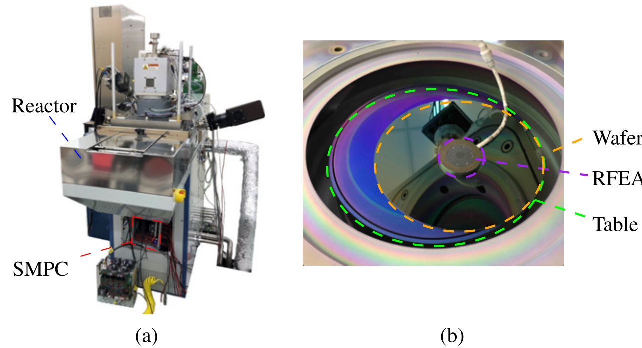

Figure 8. (a) The FlexAL system. (b) The substrate table, wafer and RFEA.

If I_{i2} is neglected, R_p turns to infinite. In practice, a sufficiently large resistance can be used for R_p during the post-discharge phase. With the value of R_p, all the circuit parameters have been extracted.

4. Experimental verification

4.1. Experimental setup

To verify the proposed EEC model and the parameter identification method, experiments were conducted with an Oxford Instruments FlexAL plasma reactor as shown in figure 8(a), which is a tool for ALD but can also be used for ALE. The RF bias generator was uninstalled and a dedicated SMPC was used to deliver the required tailored waveforms. The SMPC was coupled with the reactor table with a blocking capacitor of 2 μF. The details of the SMPC are provided in [36, 46]. An argon plasma was created with an ICP source through an automatic matching network. The plasma source can deliver up to 600 W power at 13.56 MHz. It contains a three-turn water-cooled copper coil around a cylindrical 65 mm Al_2O_3 ceramic plasma tube. The distance between the substrate and the plasma source is in the order of 25 cm. The pressure inside the reactor was kept at 2.2 mTorr. More details of the plasma reactor can be found in [47]. Four-inch and eight-inch silicon wafers with 400 nm silicon dioxide were used as the dielectric substrates.

The process of the experimental verification is depicted in figure 9. First, bias voltage waveforms with different voltage slopes were applied to the plasma reactor with a wafer on the table. The output voltage waveforms were measured with a differential voltage probe. The output currents of the power converter were measured with the current sensor. Second, the applied bias voltage waveforms and the measured output current waveforms are used for parameter identification as explained in section 3. The identified parameters are then substituted back to the EEC model for circuit simulation. The simulation was conducted in MATLAB/Simulink with SimScape toolbox.

The model used for simulation is depicted in figure 10. Compared to the EEC model depicted in figure 5, I_{i2} and C_{sh2} are neglected as explained in section 3. An ideal switch S and resistor R_{pd} are added. The status of the switch is controlled

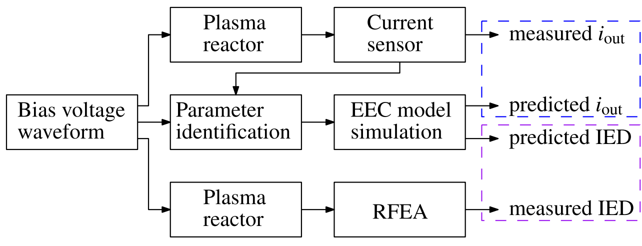

Figure 9. The process of the experimental verification.

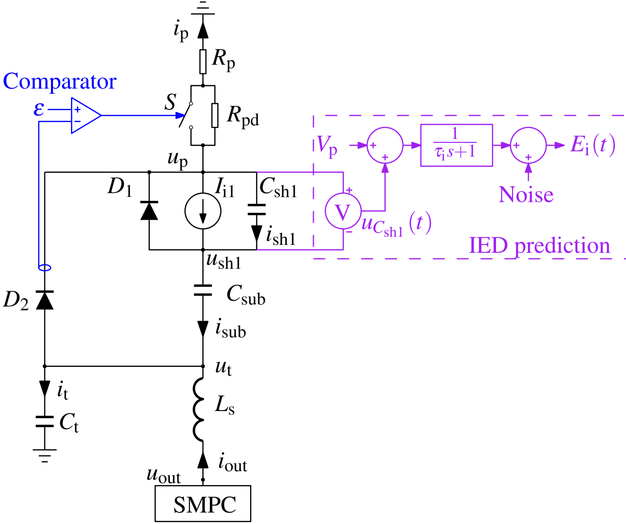

Figure 10. The circuit model used for simulation.

by the current of D_2 and the current comparator. If the current of D_2 is smaller than a small positive quantity ϵ, which equivalently means D_2 is not conducting, the output of the comparator is logic '1' and the switch S is turned on. As a result, only R_p is connected in the circuit, which is calculated by (32). Once the current of D_2 is larger than ϵ, which only happens in the post-discharge phase depicted in figure 7(d), the comparator outputs logic '0' and turns off the switch S. In this case, R_{pd} is connected in the circuit and it should be a sufficiently large value according to (35) as explained in section 3. It must be stressed that the waveforms of u_{out} used for simulation are directly from the measurements and they are measured after the blocking capacitor for simplicity. In other words, self-balancing of the output current i_{out} is not guaranteed in simulation. The electric waveforms of all the components can be predicted by circuit simulation and compared to the measured ones. In this experimental setup, only i_{out} can be measured nonintrusively and thus it was used for comparison.

Additionally, the IED can be predicted by the circuit simulation as depicted in figure 10. As explained in section 2, the ions enter the sheath with an initial energy eV_p, where the floating potential V_p is typically 20 to 40 V [9]. The ions obtain extra energy in the sheath, the value of which is determined by the instantaneous voltage of $u_{C_{sh1}}$. In practice, since the ions have a finite transit time τ_i in the sheath, they do not respond to instantaneous $u_{C_{sh1}}$. Instead, the ions respond to the averaged $u_{C_{sh1}}$ within τ_i [43]. This results in a damped effect and can be represented by a transfer function in s domain as

$$H_{damp}(s) = \frac{1}{\tau_i s + 1}. \tag{36}$$

The transit time can be approximated by the inverse of the ion plasma density frequency ω_i as

$$\omega_i = \sqrt{\frac{e^2 n_{is}}{\epsilon_0 m_i}}, \tag{37}$$

where n_{is} is the ion density at the boundary of the sheath, ϵ_0 is the vacuum permittivity and m_i is the ion mass [43]. In this work, an estimated ion density $n_{is} = 1 \times 10^{15}\ \mathrm{m}^{-3}$ is used [25] and $m_i = 40$ amu.

Furthermore, the ion energy can be affected by the collisions in the sheath, which broadens the IED [30, 48]. In practice, measurement with RFEA can also broaden the IED due to the scattering of ions on the RFEA's grids [30, 43]. These broadening effect is equivalent to a normally distributed noise defined by

$$f(E_i) = \frac{1}{\sigma\sqrt{2\pi}} \exp\left[-\frac{1}{2}\left(\frac{E_i - \mu}{\sigma}\right)^2\right], \tag{38}$$

where μ is the mean of the noise and σ is the standard deviation of the noise. In this article, μ is assumed to be zero and a typical variance $\sigma^2 = 10e^2\mathrm{V}^2$ is adopted [43].

The simulation can generate a discrete time series $\{t[1], t[2], \ldots, t[m]\}$ and the corresponding energy series $\{E_i[1], E_i[2], \ldots, E_i[m]\}$, where m is the total number of simulated moments within one repetition period and $E_i[j] (j = 1, 2, 3, \ldots, m)$ is the energy of the ions arriving at the substrate surface at time $t[j]$. If the ion flux is assumed to be constant over the period, then the normalized ion flux $P(E)$ can be approximated by

$$P(E) = \frac{1}{T} \sum_{1 \leqslant j < m, E \leqslant E_i[j] < E + \Delta E} t[j+1] - t[j], \tag{39}$$

where T is the repetition period and ΔE is the resolution of the IED measurement. Consequently, the IED can be predicted based on this circuit simulation. In order to verify the accuracy of the prediction, IEDs were measured with a commercial gridded retarding field energy analyser (RFEA) from Impedans Ltd. with a resolution $\Delta E = 1$ V as comparison. The RFEA was placed on the top of the substrate, as shown in figure 8(b). It should be noted that RFEA measurement is intrusive and can disturb the EEC model. Therefore, during the electric waveform measurement experiment, the RFEA was removed.

4.2. Parameter identification

Figure 11 shows the measured electric waveforms, including the output bias voltage and output current waveforms for the four-inch wafer with 200 W ICP power. The applied bias voltage waveforms have a repetition frequency of 100 kHz. The time percentage of the charge phase is 90% and the time percentage of the discharge phase and post-discharge phase add

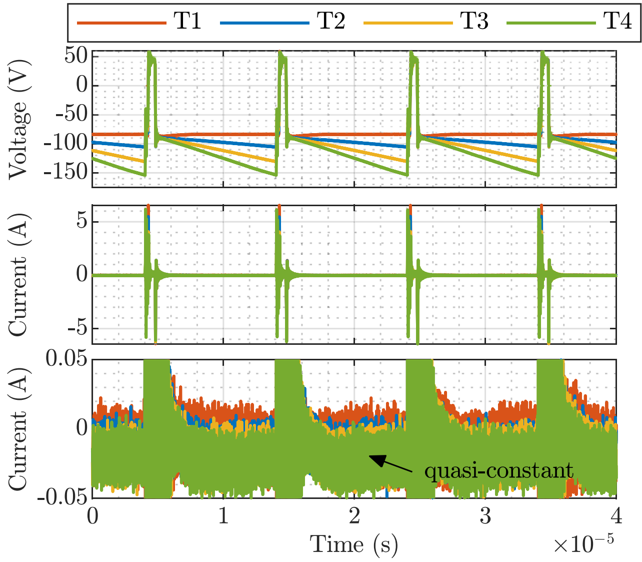

Figure 11. The measured electric waveforms, being from the top to the bottom: u_{out}, i_{out} and a zoomed-in view of i_{out}, respectively. T1, T2, T3 and T4 indicate different voltage slope rates.

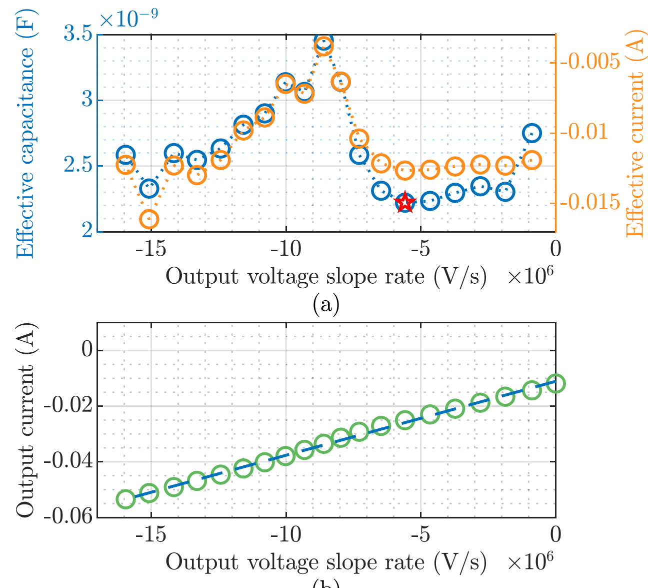

Figure 12. The measured dataset of (a) the effective capacitance C_{eff} and current I_{eff}, and (b) the output current and its linear regression at different voltage slope rates.

up to 10%. The discharge voltage V_d is fixed at 50 V and the negative voltage applied to restart the charge phase V_s is fixed at -100 V. Therefore, at the optimal operating point, the average ion energy is expected to be approximately 100 eV. The voltage slope rate is controllable and ranges from approximately 0 to -16.7×10^6 V s^{-1} in this experiment. Consequently, the peak-to-peak voltage of the bias waveforms is determined by the slope rate and ranges from 150 to 300 V. As can be seen, the output current is quasi-constant in the charge phase. When applying a different voltage slope $\dot{u}_{out}$, a different dc output current i_{out} is obtained. As analysed in section 3, the dataset of the voltage slope $\dot{u}_{out,x}$ and dc current $i_{out,x}$ can be used for identifying C_t and I_{i1}.

The measured dataset of the effective capacitance and current is shown in figure 12(a). As can be seen, C_{eff} and I_{eff} share a similar trend with the varying $\dot{u}_{out}$. The reason is that they have the same coefficient of $C_{sh1}(C_{sh1} + C_{sub})^{-1}$ according to (15) and (16). Theoretically, C_{eff} and I_{eff} should reach the minimum value at the same $\dot{u}_{out}$. However, C_{eff} reaches its minimum when $\dot{u}_{out} = -5.586 \times 10^6$ V s^{-1} as denoted by the red pentagon in figure 12(a), while I_{eff} just reaches its local minimum. When $\dot{u}_{out}$ becomes more negative, I_{eff} has a trend towards more negative value than the local minimum. This deviation is because the ion current I_{i1} is not constant as assumed in the previous analysis. Instead, I_{i1} increases when $\dot{u}_{out}$ becomes more negative, i.e. the voltage drop on the substrate sheath increases. To keep the model simple and functional within the reasonable slope rate range, the effective current is selected at the same operating point where the minimum effective capacitance is obtained. As a result, $C_t = C_{eff,x,min} = 2.22$ nF, $I_{i1} = -I_{eff,x,min} \approx 0.01265$ A.

Figure 12(b) shows the measured output current at different output voltage slopes and its linear regression. The resultant linearized equivalent capacitance and current are $C_{eq} = 2.66$ nF and $I_{eq} = 0.0111$ A, respectively. C_{sh1} and C_{sub} can be solved by (29) and (30), giving $C_{sh1} = 0.435$ nF and $C_{sub} = 3.09$ nF.

Table 1. The parameters of the EEC.

Param.	Value	Unit	Param.	Value	Unit
I_{i1}	12.65	mA	V_p	25	V
I_{i2}	0	mA	L_s	25	nH
C_t	2.22	nF	R_s	1.5	Ω
C_{sub}	3.09	nF	R_p	17.6	Ω
C_{sh1}	0.435	nF	R_{pd}	6000	Ω
C_{sh2}	0	nF	τ	50	ns

The resonance in the waveform is measured to be of $f_r = 14$ MHz. The stray inductance L_s can then be determined by (31) and is 25 nH. In addition, an equivalent series-resistance R_s is present in the loop, which is 1.5 Ω. Apart from these, selecting $\tau = 50$ ns as introduced in section 3, R_p can be calculated by (32) and is 17.6 Ω. The value of R_{pd} should be sufficiently large since I_{i2} is neglected as explained in section 3. In this case, $R_{pd} = 6000$ Ω is sufficient. The value of R_{pd} affects i_{out} during the post-discharge phase, which is not of interest. Therefore, it is not required to be very accurate. In short, all the parameters are identified and summarized in table 1.

4.3. Electric waveform and ion energy distribution prediction

By substituting the identified parameters back to the EEC model and applying the same bias voltage waveforms to it for circuit simulation, the electric waveforms can be predicted. Figure 13 shows the predicted waveforms at the optimal operating point from the circuit simulation based on the EEC model. Both the sheath surface potential u_{sh1} and the ion energy E_i are quasi-constant during the charge phase. The

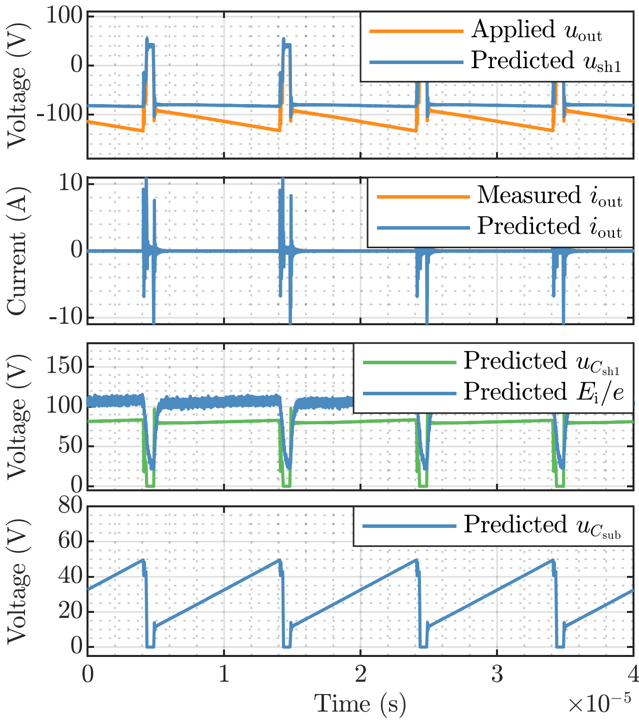

Figure 13. The predicted electric waveforms from the circuit simulation based on the EEC model. The measured and predicted i_{out} are almost overlapping.

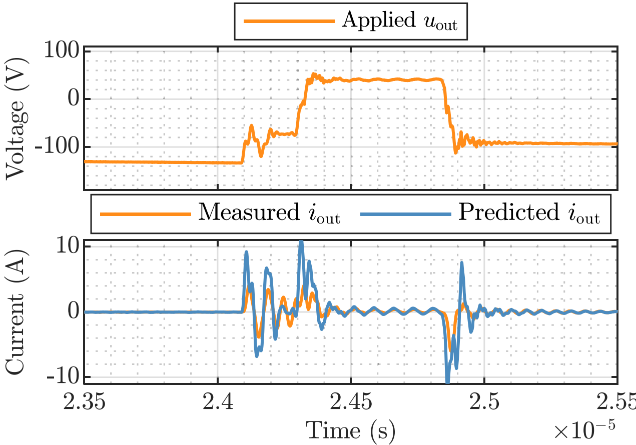

Figure 14. A zoomed-in view around the discharge phase of the predicted electric waveforms from the circuit simulation based on the EEC model.

waveform of $u_{C_{sh1}}$ and $u_{C_{sub}}$ cannot be measured with this experimental setup but the predicted results are in line with the measured results demonstrated in [30]. Figure 14 shows a zoomed-in view around the discharge phase of the waveforms. As can be seen from figures 13 and 14, the predicted i_{out} matches the measured i_{out} generally in transient behaviour, magnitude and resonant frequency.

Additionally, the IED can be predicted based on the predicted waveform of E_i according to (39), as shown in figure 15. Similarly, by applying the same bias voltage waveform to both the simulation model and the plasma reactor with an RFEA

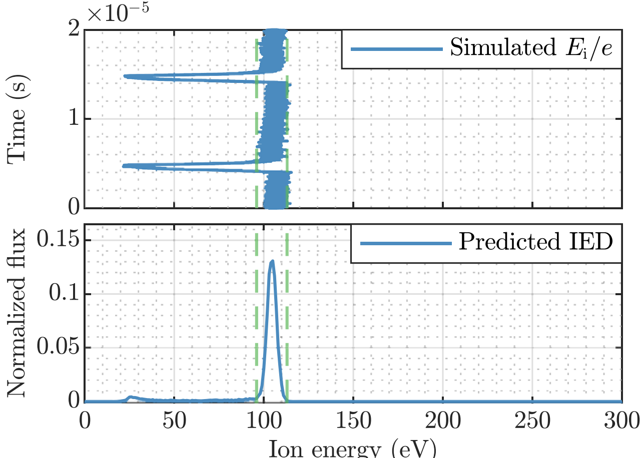

Figure 15. The IED prediction from the waveform of E_i.

presented, the predicted and measured normalized IED can be compared. Figure 16 shows comparisons of the predicted and measured results for different voltage slopes. The predicted results can generally represent the trend of the measured ones. Furthermore, the full width at-half-maximum (FWHM) and the average energy at different voltage slope rates from both the simulations and measurements are compared, as shown in figure 17. On the one hand, the predicted IEDs accurately find the optimal slope rate which leads to the minimum FWHM. On the other hand, the predicted average values of the ion energy are within 10 eV difference compared to the measurements. It should be noted that the IED can only be measured with RFEA, which is interactive with the plasma processing and IEDs. The IED in the case without RFEA is inherently different from that with RFEA. This might contribute to the deviation of the comparison.

4.4. Discussion

The same experiments were also carried out for the eight-inch wafer and at different ICP powers. The resultant identified parameters are shown in table 2. As can be seen from the table, C_t is uniform and around 2.3 nF for different wafers with different ICP powers, which makes sense because both the area of and the distance between the table and reactor wall remain unchanged. The extracted C_{sub} is of several nanofarads for both applied wafers. However, the extracted C_{sub} of the same wafer is expected to be the same with different ICP powers while they deviate in the results. The reason is that C_{sub} is calculated based on multiple extracted parameters, including C_{sh1}, I_{eq} and I_{i1}, according to (30). Since inaccuracy occurs when identifying each parameter, it will be accumulated on C_{sub}, i.e. the identification of C_{sub} is more sensitive.

The identified values of C_{sh1} are around 0.4 nF for different wafers with different ICP powers. Furthermore, the current I_{i1} has a positive correlation with the ICP power. It is interesting to note that even the eight-inch wafer is four times the area of the four-inch wafer, the value of their C_{sh1} and I_{i1} are still similar when employing the same ICP power. This similarity is due to the neglection of the C_{sh2} and I_{i2}. In (24), the

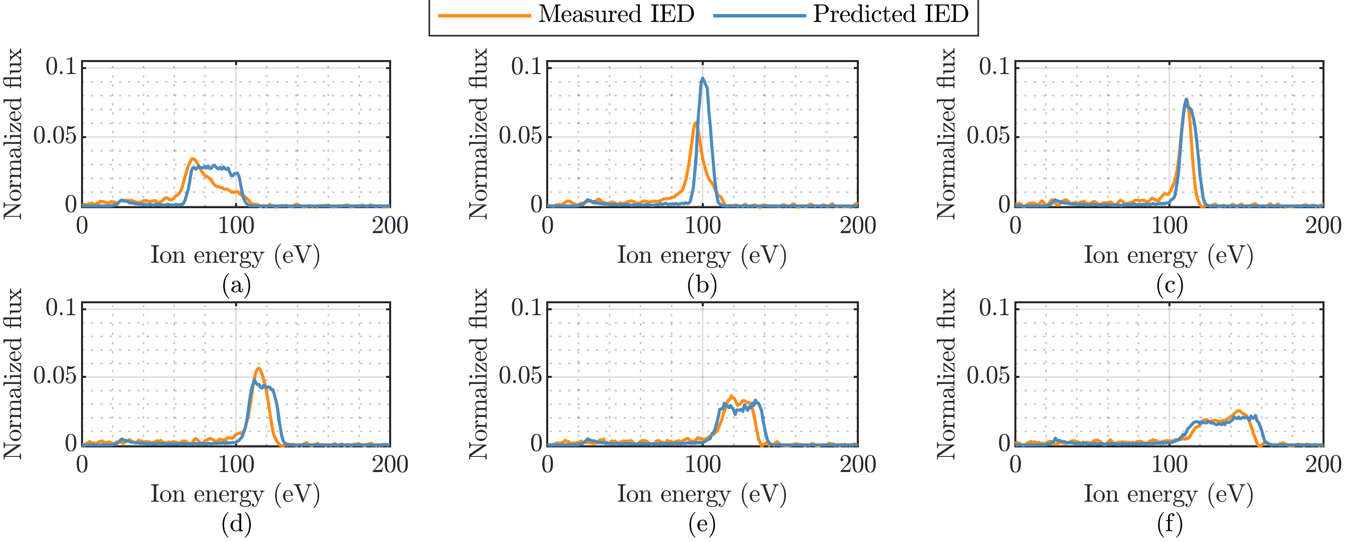

Figure 16. Comparison of the predicted and measured normalized IED for the four-inch wafer with 200 W ICP power at voltage slope rate of (a) 0.056×10^4 V s^{-1}, (b) -3.023×10^{-6} V s^{-1}, (c) -5.722×10^6 V s^{-1}, (d) -6.753×10^6 V s^{-1}, (e) -7.983×10^6 V s^{-1}, and (f) -9.982×10^6 V s^{-1}.

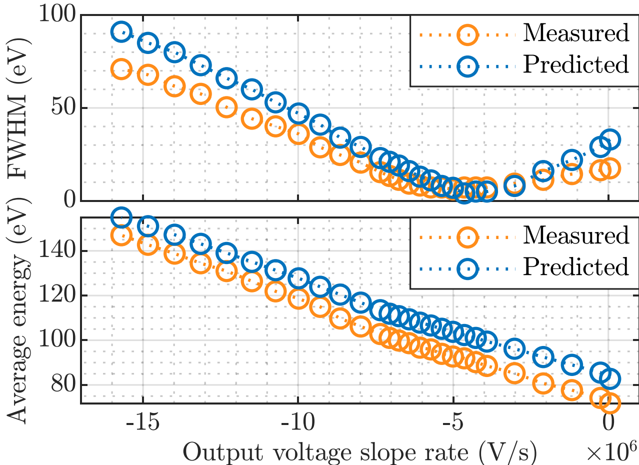

Figure 17. Comparison of the predicted and measured FWHM and average energy for the four-inch wafer with 200 W ICP power at different voltage slope rates.

Table 2. The identified parameters of the plasma reactor with different wafers at different ICP powers.

Wafer	Four-inch		Eight-inch	
ICP power (W)	200	600	200	600
C_t (nF)	2.22	2.36	2.31	2.34
C_{sub} (nF)	3.09	4.35	2.84	3.65
C_{sh1} (nF)	0.435	0.386	0.409	0.402
I_{i1} (mA)	12.65	15.26	11.99	15.24

equivalent capacitance C_{eq} is defined and in (27), its value is obtained by linear regression, as shown in figure 12(b). This value is obtained based on the simplified system described by (19) which neglects C_{sh2} and I_{i2} in the real system as described by (14). In other words, the real definition of C_{eq} is

$$C_{eq} = \frac{C_{sh1} C_{sub}}{C_{sh1} + C_{sub}} + C_{sh2} + C_t \approx C_{sh1} + C_{sh2} + C_t. \quad (40)$$

As a result, the previously identified C_{sh1} is actually the sum of real $C_{sh1} + C_{sh2}$. Similarly, the previously identified I_{i1} is actually the sum of real $I_{i1} + I_{i2}$ according to (21). Because the total exposed area (equal to the total area of the solid part and the gridded part of the table as depicted in figure 1) is constant, both the sum of the sheath capacitance and ion current should roughly maintain similar values even when a different wafer is used. This effect also evidences that there is an extra sheath between the plasma and the exposed part of the table.

To summarize, in this section, the parameters of the EEC model are identified based on the experimental measurements. The EEC model is simulated by using the identified parameters. Both the predicted electric waveforms and IEDs align well with the measured results. The same experiments were conducted for two different wafers with different ICP powers while similar results were obtained, demonstrating the wide application scope of the proposed method. The possible reasons for the deviation between the simulations and measurements are also analysed.

5. Conclusion

The equivalent electric circuit (EEC) model of the plasma reactor is essential for circuit simulation and bias waveform optimization in atomic scale processing with tailored waveform biasing. Traditional EEC models are typically used for RF biasing and not suitable for tailored waveform biasing, mainly because the capacitors in the circuit cannot be rapidly and completely discharged during the discharge phase. In this article, an improved EEC model of the plasma reactor is introduced. The improved EEC model simplifies the plasma by a resistor

thus providing a fast discharge path for the capacitors. Meanwhile, it adds another sheath between the bulk plasma and the exposed part of the reactor table, being the table sheath, so that all the capacitors can be fully discharged to zero voltage. In tailored waveform biasing, there are three different processing phases including the charge phase, the discharge phase, and the post-discharge phase. The proposed model is analysed in details during all of these phases.

Additionally, a parameter identification method is proposed to fulfil the simulation of the EEC model on the circuit level. It is fully based on electrical measurements, using only the waveforms of output voltage and current. Both waveforms can be easily measured and the measurements are nonintrusive to the process. The identification method linearizes all the components, including the sheath capacitors and currents. With the proposed EEC model and parameter identification method, the electric waveforms and IEDs can be predicted by circuit simulation. Experiments have been conducted for verification. The alignment between the predictions and measurements underlines the correctness and accuracy of the proposed EEC model and parameter identification.

This research bridges the gap between plasma processing and bias power converter design. It gives an electrically equivalent description of the plasma reactor and provides more insight into the process from the electrical engineering's perspective. Accordingly, the EEC can be used to design and optimize the SMPC for electrical engineers, thus significantly improve the process efficiency. Meanwhile, a well-designed bias converter also enhances tailored waveform biasing in the future. Moreover, it poses a new way for plasma parameter identification, with which linearized plasma parameters, such as sheath capacitance and ion current, can be obtained nonintrusively. Additionally, the IEDs can be predicted with circuit simulation, which can be a supplement and substitute to the traditional plasma simulation method like PIC, enjoying the advantage of considerably reduced computation time. This model might also be used for bias waveform optimization and IED tailoring.

The proposed model is expected to be compatible with other bias waveforms like RF biasing and pulse-shaped biasing but requires further experimental validation. For the future research, it is recommended to improve the accuracy of the parameter identification by taking nonzero C_{sh2} and I_{i2} into consideration.

Data availability statement

The data generated and/or analysed during the current study are not publicly available for legal/ethical reasons but are available from the corresponding author on reasonable request.

Acknowledgments

The authors gratefully acknowledge the financial support of Prodrive Technologies BV and the assistance from Javier Escandon-Lopez, Erik Heijdra, Anton Driessen, Koen Buskes, Pedro Dans, Yuri Verstappen, Dr. Tahsin Faraz and Dr. Shashank Balasubramanyam. The work by Adriaan J M Mackus and Wilhelmus M M (Erwin) Kessels is part of the research program HTSM with Project No. 17124, which is financed by The Netherlands Organization for Scientific Research (NWO).

ORCID iDs

Qihao Yu (余骑浩) https://orcid.org/0000-0001-5318-434X
Erik Lemmen https://orcid.org/0000-0002-4471-1352
Bas Vermulst https://orcid.org/0000-0001-9019-6147
Adriaan J M Mackus https://orcid.org/0000-0001-6944-9867
Wilhelmus M M (Erwin) Kessels https://orcid.org/0000-0002-7630-8226
Korneel Wijnands https://orcid.org/0000-0003-3302-1599

References

[1] Clark R, Tapily K, Yu K h, Hakamata T, Consiglio S, O'Meara D, Wajda C, Smith J and Leusink G 2018 *APL Mater.* **6** 058203
[2] Faraz T, Roozeboom F, Knoops H C M and Kessels W M M 2015 *ECS J. Solid State Sci. Technol.* **4** N5023–32
[3] Kanarik K J, Lill T, Hudson E A, Sriraman S, Tan S, Marks J, Vahedi V and Gottscho R A 2015 *J. Vac. Sci. Technol.* A **33** 020802
[4] Faraz T, Arts K, Karwal S, Knoops H C and Kessels W M 2019 *Plasma Sources Sci. Technol.* **28** 24002
[5] Kanarik K J *et al* 2017 *J. Vac. Sci. Technol.* A **35** 05C302
[6] Barnat E V, Lu T M and Little J 2001 *J. Appl. Phys.* **90** 4946–50
[7] Sansonnens L, Pletzer A, Magni D, Howling A A, Hollenstein C and Schmitt J P M 1997 *Plasma Sources Sci. Technol.* **6** 170–8
[8] Perret A, Chabert P, Booth J P, Jolly J, Guillon J and Auvray P 2003 *Appl. Phys. Lett.* **83** 243–5
[9] Lieberman M A and Lichtenberg A J 2005 *Principle of Plasma Discharges and Materials Processing* 2nd edn (New York: Wiley)
[10] Goto H H, Löwe H and Ohmi T 1992 *J. Vac. Sci. Technol.* A **10** 3048–54
[11] Goto H, Lowe H D and Ohmi T 1993 *IEEE Trans. Semicond. Manuf.* **6** 58–64
[12] Bi Z H, Liu Y X, Jiang W, Xu X and Wang Y N 2011 *Curr. Appl. Phys.* **11** S2–8
[13] Lee J K, Manuilenko O V, Babaeva N Y, Kim H C and Shon J W 2005 *Plasma Sources Sci. Technol.* **14** 89–97
[14] Heil B G, Czarnetzki U, Brinkmann R P and Mussenbrock T 2008 *J. Phys. D: Appl. Phys.* **41** 165202
[15] Czarnetzki U, Schulze J, Schüngel E and Donkó Z 2011 *Plasma Sources Sci. Technol.* **20** 024010
[16] Schüngel E, Eremin D, Schulze J, Mussenbrock T and Czarnetzki U 2012 *J. Appl. Phys.* **112** 53302
[17] Lafleur T 2015 *Plasma Sources Sci. Technol.* **25** 13001
[18] Krüger F, Wilczek S, Mussenbrock T and Schulze J 2019 *Plasma Sources Sci. Technol.* **28** 075017
[19] Hartmann P *et al* 2021 *J. Phys. D: Appl. Phys.* **54** 255202
[20] Rauf S 2000 *J. Appl. Phys.* **87** 7647–51
[21] Qin X V, Ting Y H and Wendt A E 2010 *Plasma Sources Sci. Technol.* **19** 065014
[22] Economou D J 2013 *J. Vac. Sci. Technol.* A **31** 050823
[23] Agarwal A and Kushner M J 2005 *J. Vac. Sci. Technol.* A **23** 1440–9

[24] Zhenfeng D, Weigang H and Younian W 2006 *Plasma Sci. Technol.* **6** 2549–58
[25] Profijt H B, van de Sanden M C M and Kessels W M M 2013 *J. Vac. Sci. Technol.* A **31** 01A106
[26] Barnat E V and Lu T M 2002 *Phys. Rev.* E **66** 056401
[27] Shin H, Zhu W, Xu L, Donnelly V M and Economou D J 2011 *Plasma Sources Sci. Technol.* **20** 055001
[28] Ui A, Hayashi H, Sakai I, Kaminatsui T, Ohiwa T, Yamamoto K and Kikutani K 2016 *J. Vac. Sci. Technol.* A **34** 031301
[29] Wang S B and Wendt A E 2000 *J. Appl. Phys.* **88** 643–6
[30] Kudlacek P, Rumphorst R F and van de Sanden M C M 2009 *J. Appl. Phys.* **106** 073303
[31] Martin I T, Wank M A, Blauw M A, van Swaaij R A C M M, Kessels W M M and van de Sanden M C M 2010 *Plasma Sources Sci. Technol.* **19** 015012
[32] Liu Z, Dai Z, He C and Wang Y 2015 *Plasma Sci. Technol.* **17** 560–6
[33] Faraz T, Verstappen Y G, Verheijen M A, Chittock N J, Lopez J E, Heijdra E, Van Gennip W J, Kessels W M and MacKus A J 2020 *J. Appl. Phys.* **128** 213301
[34] Sobolewski M A, Olthoff J K and Wang Y 1999 *J. Appl. Phys.* **85** 3966
[35] Mizutani N and Hayashi T 2001 *J. Vac. Sci. Technol.* A **19** 1298–303
[36] Yu Q, Lemmen E, Wijnands K and Vermulst B 2020 A switched-mode power amplifier for ion energy control in plasma etching *2020 22nd Eur. Conf. Power Electron. Appl. (EPE'20 ECCE Eur.)* (IEEE) pp P.1–P.8
[37] Dai Z L and Wang Y N 2002 *J. Appl. Phys.* **92** 6428–33
[38] Gahan D, Daniels S, Hayden C, Scullin P, O'Sullivan D, Pei Y T and Hopkins M B 2012 *Plasma Sources Sci. Technol.* **21** 8
[39] Saikia P, Bhuyan H, Escalona M, Favre M, Bora B, Kakati M, Wyndham E, Rawat R S and Schulze J 2018 *J. Appl. Phys.* **123** 183303
[40] Brouk V, Hoffman Daniel J, Carter D and Kovalevskii D 2014 Wide dynamic range ion energy bias control; fast ion energy switching; ion energy control and a pulsed bias supply; and a virtual front panel *Patent* WO2014036000A1
[41] Yu Q, Lemmen E and Vermulst B J D 2021 Determining an optimal ion energy for plasma processing of a dielectric substrate *Patent* WO2021064110
[42] Yu Q, Lemmen E, Wijnands C G E and Vermulst B 2021 Model and verification of a plasma etching reactor with a switched-mode power converter *2021 IEEE 12th Energy Convers. Congr. Expo.—Asia* (IEEE) pp 568–73
[43] Diomede P, Economou D J and Donnelly V M 2012 *J. Appl. Phys.* **111** 123306
[44] Song S H and Kushner M J 2014 *J. Vac. Sci. Technol.* A **32** 021306
[45] Chen F F and Chang J P 2003 *Lecture Notes on Principles of Plasma Processing* (Berlin: Springer)
[46] Driessen A W 2020 Voltage waveform generator for plasma processing apparatuses *Patent* WO2020216741
[47] Heil S B S, van Hemmen J L, Hodson C J, Singh N, Klootwijk J H, Roozeboom F, van de Sanden M C M and Kessels W M M 2007 *J. Vac. Sci. Technol.* A **25** 1357
[48] Bogdanova M, Lopaev D, Rakhimova T, Voloshin D, Zotovich A and Zyryanov S 2021 *Plasma Sources Sci. Technol.* **30** 075020